TUDelft

Delft University of Technology

Pushing nanomaterials up to the kilogram scale – An accelerated approach for synthesizing antimicrobial ZnO with high shear reactors, machine learning and high-throughput analysis

Jose, Nicholas A.; Kovalev, Mikhail; Bradford, Eric; Schweidtmann, Artur M.; Chun Zeng, Hua; Lapkin, Alexei A.

Citation (APA)
Jose, N. A., Kovalev, M., Bradford, E., Schweidtmann, A. M., Chun Zeng, H., & Lapkin, A. A. (2021). Pushing nanomaterials up to the kilogram scale – An accelerated approach for synthesizing antimicrobial ZnO with high shear reactors, machine learning and high-throughput analysis. *Chemical Engineering Journal*, *426*, Article 131345. https://doi.org/10.1016/j.cej.2021.131345

Important note
To cite this publication, please use the final published version (if applicable).
Please check the document version above.

Pushing nanomaterials up to the kilogram scale - an accelerated approach for synthesizing antimicrobial ZnO with high shear reactors, machine learning and high-throughput analysis

Nicholas A. Jose,*†‡ Mikhail Kovalev†, Eric Bradford‖, Artur M. Schweidtmann¦, Hua Chun Zeng†§, Alexei A. Lapkin†‡

† Cambridge Centre for Advanced Research and Education in Singapore Ltd. 1 Create Way, CREATE Tower #05-05, 138602 Singapore

‡ Department of Chemical Engineering and Biotechnology, University of Cambridge, Philippa Fawcett Drive, Cambridge CB3 0AS, UK

‖ Ecological Systems Design, ETH Zurich, John-von-Neumann-Weg 9 8093 Zürich, Switzerland

¦ Department of Chemical Engineering, Delft University of Technology, Van der Maasweg 9, Delft 2629 HZ, The Netherlands

§ Department of Chemical and Biomolecular Engineering, Faculty of Engineering, National University of Singapore, 10 Kent Ridge Crescent, Singapore 119260

Corresponding Author: Nicholas A. Jose (nj278@cam.ac.uk)

ABSTRACT: Novel materials are the backbone of major technological advances. However, the development and wide-scale introduction of new materials, such as nanomaterials, is limited by three main factors—the expense of experiments, inefficiency of synthesis methods and complexity of scale-up. Reaching the kilogram scale is a hurdle that takes years of effort for many nanomaterials. We introduce an improved methodology for materials development, combining state-of-the-art techniques—multi-objective machine learning optimization, high yield microreactors and high throughput analysis. We demonstrate this approach through the optimization of ZnO nanoparticle synthesis, simultaneously targeting high yield and high antibacterial activity. In fewer than 100 experiments, we developed a 1 kg day^{-1} continuous synthesis for ZnO (with a space-time-yield of 62.4 kg day^{-1} m^{-3}), having an antibacterial activity comparable to hydrothermally synthesized nano-ZnO and cetrimonium bromide. Following this, we provide insights into the mechanistic factors underlying the performance-yield tradeoffs of synthesis and highlight the need for benchmarking machine learning models with traditional chemical engineering methods. Methods for increasing model accuracy at steep pareto fronts, in this case at yields close to 1 kg per day, should also be improved. To project the next

steps for process scale-up and the potential advantages of this methodology, we conduct a scalability analysis in comparison to conventional batch production methods, in which there is a significant reduction in degrees of freedom. The proposed method has the potential to significantly reduce experimental costs, increase process efficiency and enhance material performance, which culminate to form a new pathway for materials discovery.

Graphical Abstract
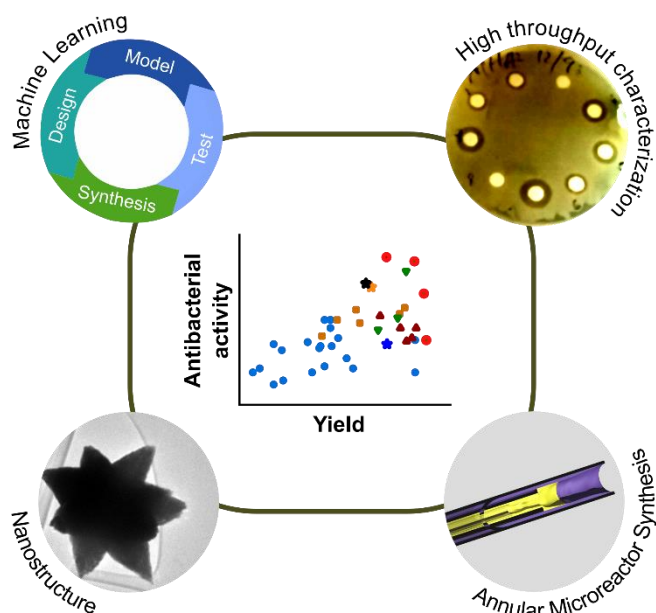
1   INTRODUCTION

Material innovation is a stepping-stone for technology development. Yet, development and commercialization of new materials is significantly limited by the expense, time and experience required. The typical time to bring a novel material to market is 10 to 20 years [1]. For nanomaterials, which are touted as next generation materials for many industries, developmental and production-related issues severely limit their commercial potential [2-7]. Synthetic methods reported in literature are often too expensive or too hazardous to directly translate to the industrial scale. Key fundamental knowledge is also lacking. Recent studies have revealed complex relationships between material formation and mass transfer characteristics, such as hydrodynamics, which change significantly during scale-up [8]. Furthermore, commercialization requires the optimization of multiple competing criteria, such as cost and specific performance, which are often neglected in published research studies and patents. The target of creating an accelerated methodology for the development and mass-production of new materials has become especially urgent in times of

increasing climate change, epidemics and economic instability. Several national efforts have already been initiated to tackle this challenge, including the Accelerated Materials Development for Manufacturing Programme (SG) [9] and Materials Genome Initiative (USA)[3]. In this work we present an accelerated methodology for materials development and scale-up, and demonstrate it through a scalable route to functional nano ZnO materials.

Materials development and scale-up requires an exhaustive amount of experimentation to understand the multivariable material-processing-property relationship. Scaling-up production from the laboratory (mg-g) to the pilot (kg-ton) and production scale (multi-ton) is often heuristic or empirical, amplifying the complexity and expense of development. Although mechanistic model-based scale-up is possible, accurate kinetic models of nanomaterial formation are both computationally expensive and difficult to derive. Several variations of larger equipment must be purchased, lab protocols must be re-evaluated, engineering parameters must be determined at each stage, and the labor required increases with each scale and experiment. While moving from each scale in this segregated, sequential fashion (i.e. the "stage-gate" approach) can lower risk, it involves large teams, which frequently lack proper information exchange [10].

Pilot-scale trials are the most critical step in scale-up, at which optimal engineering parameters for large-scale production are determined. Failures at the pilot scale are significantly more expensive than at the lab scale; work reverts to the laboratory and further investment in development is discouraged. Furthermore, the low availability of pilot production lines for nanomaterials, lack of industry technology readiness and poor knowledge of pilot processing amongst small-medium enterprises (SMEs) have recently been noted as barriers to the development of innovative material ecosystems [2].

Several tools have recently been developed to accelerate development. Coupling computational modelling with high-throughput experimentation can accelerate design and discovery [3, 11]. Machine-learning (ML) algorithms can increase the efficiency of data analysis and optimization [12, 13]. However, experimental applications of ML in materials optimization are typically focused on batch, mg-g scale synthesis. Conventional batch synthesis is not readily scalable because not all mass transfer parameters can be preserved when scaling to larger volumes [14].

Recently, the scalability of wet chemical synthesis has increased through the development of new processing techniques. Annular microreactors [15], spinning disk reactors [16], supercritical flow reactors [17] and helical flow

reactors [18] can increase space-time-yield (STY – reaction yield per unit time per unit volume) by orders of magnitude while retaining control over nanoparticle size. Micromixers also provide precise control over mass transfer, which nanomaterials are sensitive to [19]. In contrast to conventional scaling of stirred tank reactors by increasing reactor volume ("scale-out"), micromixers are typically scaled by increasing the number of reactors in parallel ("number-up") to conserve mass transfer characteristics [20]. In addition to the dimensionless parameters that have become the mainstay of scale-up methodology, hydrodynamic shear rate and residence time are also essential factors to consider in process intensification and scale-up of anisotropic nanoparticle production, for example, in the synthesis of layered double hydroxides [21], graphene [22] and titania nanotubes [23].

To approach the issues of scalability, efficiency and process complexity in nanomaterials development, a cross-disciplinary toolbox of acceleration techniques is needed. In this study we incorporated three tools: scalable processing technology, surrogate-based multi-objective optimization, and high-throughput testing. By doing this, we circumvented the classical stage-gate approach of product development, which is often upset by repeated failures and miscommunication between entities at different scales, and implement an "agile-inspired" development methodology, seen in Figure 1.
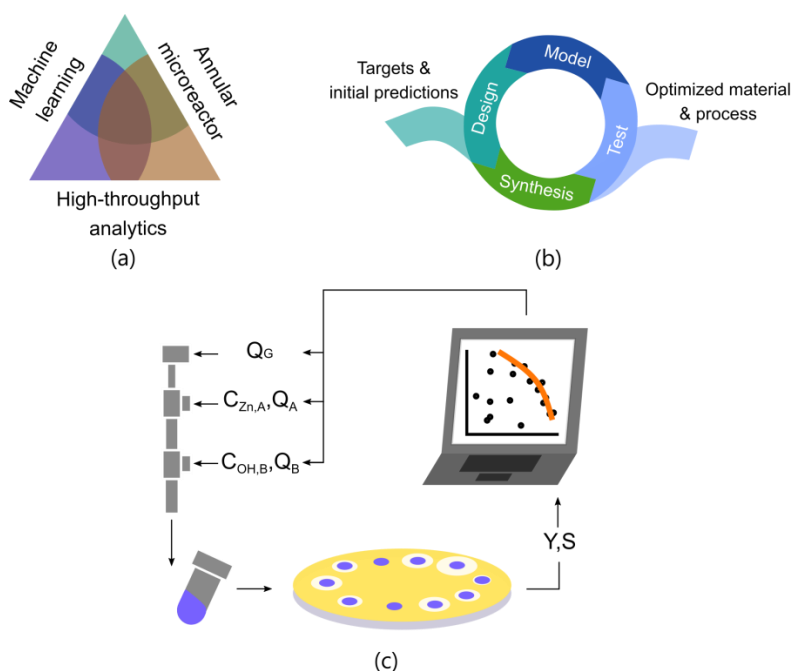

Figure 1. Development methodology utilizing multiple acceleration tools (a) and an agile-inspired development strategy (b), illustrated schematically in (c).

To demonstrate the potential of the proposed approach in a case study, we developed a kg-per-day process for manufacture of highly active antimicrobial ZnO particles. ZnO possesses well-known antimicrobial properties, which stem from its surface activity, release of Zn^{2+} and catalyzed production of radical oxygen species [24, 25], which are correlated to its nanostructure [26, 27]. As a model system, ZnO possesses many of the challenges common to nanomaterial synthesis – morphological diversity, hard-to-scale published synthesis methods, and a complex performance-property relationship. Cost-effective antibacterial nanomaterials also have high social importance due to the rise of antibiotic resistance and high risk of surface-transmitted disease in public areas.

To synthesize ZnO in a scalable manner, we used annular microreactor synthesis (AMS), which was recently developed for the precise and high yield synthesis of two-dimensional materials, including layered double hydroxides[15] and metal-organic frameworks [28] with low clogging. Reagents and reactor conditions, including the shear rate and residence times, were varied to optimize antimicrobial efficiency and production efficiency. We employed the Thompson Sampling Efficient Multi-Objective algorithm (TSEMO); an approach for the simultaneous optimization of competing objectives with limited experimental evaluations [29-31]. Antimicrobial activity was assessed through the disk-diffusion test for inhibition of *Escherichia coli* growth, which allows a large number of samples to be tested in parallel. Mechanistic insights on ZnO synthesis with this approach were then drawn by characterizing a limited set of materials *post*-optimization. We then assessed this approach by comparing development time, safety, complexity and scalability to previously-reported continuous and batch processes.

2   MATERIALS AND METHODS

2.1   ZnO synthesis and yield

Synthesis of ZnO was conducted in an annular microreactor [15, 28], which was assembled with three quartz capillary tubes from VitroCom (Tube 1 = 0.30 mm inner diameter x 0.4 mm outer diameter x 100 mm long, T2 = 0.50 mm inner diameter x 0.7 mm outer diameter x 100 mm long, and T3 = 1 mm inner diameter x 1.2 mm outer diameter x 100 mm long) in a "tube-in-tube" coaxial fashion. Stainless steel tee unions with 1/16" diameter tube compression fittings (Swagelok) with graphite ferrules (Restek) were used to connect the fittings stainless steel fittings and quartz tubes. A custom-built mount was used to precisely align the capillaries and fittings, which was evaluated visually using a portable microscope and magnifying glass. The length of the region in which reagents mix in the outermost tube was 50 mm.

A KDS Legato Dual Syringe Pump using disposable plastic 10 mL syringes was used to deliver liquid reagents to T2 and T3. The flow of filtered, compressed dried air through T1 was controlled using a Sierra SmartTrak C50L Mass Flow controller (20 L min^{-1} max, 2% accuracy).

Reagent solutions of Zn-reagent ("A") and alkaline reagent ("B"), prepared in the same solvent (either water or ethanol), were pumped simultaneously at equal flowrates into the outermost tubes (T2 and T3) of the annular microreactor while the compressed dried air flowed at high velocity through the innermost tube (T1). Solution A was pumped through T2 and solution B through T3. The resulting precipitates were centrifuged at 6,000 rpm and rinsed three times in water or ethanol, ensuring that the final suspensions were of the same volume as their original reaction slurry. After rinsing, the solids content of the suspension and the corresponding dry-equivalent solid yield were determined gravimetrically by evaporating 1 mL of purified slurry in pre-weighed glass vials at 110 °C. Three replicates were performed per experimental condition, using the average result for optimization. No unexpected or unusually high safety hazards were encountered.

Shear rates, pressure drops and velocities within the mixing region were calculated using the empirical model of Han *et al.* for wall stresses in gas-liquid annular flows for laminar and turbulent gas flows in tubes of 1 mm in diameter [32]. The averaged residence time (τ_R) was calculated using Equation 1, where is the estimated average residence time (s), l is the length of the mixing region (m) and U_L is the liquid film velocity (m s^{-1}).

(1) $\qquad \tau_R = \frac{l_3}{U_L}$

The mean rate of energy dissipation per unit mass ε (m^{2}s^{-3} or W·kg^{-1}) was calculated using Equation 2, where ΔP is the change in pressure (Pa) and ρ is the liquid density (998 kg·m^3).

(2) $\qquad \varepsilon = \frac{\Delta P}{\rho \tau_R}$

The characteristic mixing time was then estimated from the relationship between the rate of energy dissipation and micromixing time for vortex engulfment [33], which is given by Equation 3, where τ_E is the characteristic micromixing time (s) and υ is the kinematic viscosity (m^{2}s^{-1}).

(3) $\qquad \tau_E = 17.2\sqrt{\upsilon/\varepsilon}$

2.2   Disk-diffusion test for antimicrobial activity

In an adaptation of the Kirby-Bauer Disk Diffusion Test [34], *Escherichia coli* (ATCC 8739-BioRev) grown in Nutrient Broth (BioRev) at 37 °C was dispersed in 0.85% saline solution to an optical density of 0.1 at a wavelength of 600 nm. This dispersion was then spread on Mueller Hinton Agar (VWR) in petri dishes with sterile cotton swabs.

30 μL of 2.5 wt.% ZnO suspensions were dropped onto disks of cellulose filter paper measuring 6 mm in diameter and dried. These disks were then placed face-down onto the inoculated plates, which were then incubated at 37 °C for 16-18 hours. The diameter of the clear "inhibition" zone around each disk was measured. A ZnO control sample, which was known to reduce *E.Coli* colony forming units by >99%, supplied by A*STAR SIMTech and synthesized according to reference [35], and a 2.5% solution of cetyltrimethylammonium bromide (CTAB – Merck), a known bactericide, were used as controls for each test. The average diameter of the control and CTAB were 9.9 ± 1.7 and 9 mm ± 0, respectively. The antibacterial performance score, which represents the difference between the sample inhibition area and control inhibition areas, is given as $S = D_S - D_C$, where D_s is the sample inhibition zone diameter and D_C is the inhibition zone diameter. For regions with no inhibition $D_S = 6$ mm, the diameter of the filter paper. Due to the variability of the method, three replicates were performed for each ZnO sample. Testing was done at a frequency of one batch (six samples) per day.

2.3   Experimental Design and Optimization

The experimental design methodology, shown schematically in Figure 2, consists of the following steps:

1) Antibacterial performance S in the disk-diffusion agar method with *E.Coli* as test bacteria (in units of mm) and reactor time yield Y (in g of dry equivalent ZnO per minute) were selected as objectives.

2) 25 papers (references [25-27, 35-57]) were surveyed for wet-chemical precipitation methods that are compatible with annular microreactor synthesis to determine relevant synthesis variables. These synthesis variables were determined to be the zinc reagent anion (nitrate, sulfate, acetate or chloride), the alkaline reagent (NaOH or KOH), zinc and alkaline reagent concentrations and mixing intensity.

3) These variables were screened in a blocked factorial design to reduce the number of redundant variables and establish valid ranges on conditions for optimization, which amounted to 26 different synthesis conditions. From the results of these experiments, we saw that zinc reagent anions and alkaline reagent cations did not have significantly different effects on yield and performance. $Zn(NO_3)-6H_2O$ (reagent A) and KOH (reagent B) were selected as reagents,

7

and water was selected as the solvent due to its lower cost and less hazardous nature compared to most organic solvents. The four selected input variables and their ranges are summarized in Table 1.

Table 1 Optimization variables and their bounds.

Variable name	Unit	Lower bound	Upper bound
Concentration, Zn^{2+} in A ($C_{Zn,A}$)	M	0.1	1
Ratio KOH: Zn^{2+} ($R_{KOH:Zn}$)	-	1.5	3
Total liquid flowrate (Q_L)*	mL min^{-1}	8	20
Total air flowrate (Q_G)	L min^{-1}	0.5	3

* The flowrates of A and B are equal ($Q_A = Q_B$).

4) Three iterations of the Thompson Sampling Efficient Multi-Objective algorithm (TSEMO) were performed. An initial set of 20 experimental conditions was generated *via* Latin hypercube sampling (LHS) [58]. From this initial experimental dataset, TSEMO fits Gaussian process surrogate models (GPs) for each objective; from these surrogate models, the next set of experimental conditions that would best minimize model uncertainty and maximize the objectives (*i.e.* best approximate the Pareto front) is computed. After these conditions are experimentally tested, the optimization process is repeated until a specified maximum number of iterations has been reached. In this study, the covariances of the GP models were modelled by Matérn kernels of the 1/2 and 3/2 orders for yield and antibacterial score GPs respectively. For a more detailed description of TSEMO we recommend the reader to consult reference [29]. TSEMO code used for optimization was written in MATLAB and is available at [https://github.com/Eric-Bradford/TS-EMO].

5) To further extend our approach, we have included another decision-making step—if the optimal conditions to reach the target objectives have not been determined, the process must revert back to step 2 and iterate. In this study, three iterations were used with 6 experimental conditions per iteration, were found to be sufficient. Hence, TSEMO chooses overall 18 experimental conditions to be carried-out.

6) To assess the Gaussian Process (GP) model quality, leave-one-out cross-validation (LOO-CV) was performed, in which the model was trained on the experimental dataset 38 times, each time leaving one data point out for prediction [59]. To assess GP model predictions, we use the average absolute error (ε), which is defined in Equation 3, where i is a sample point, $\hat{y}_i$ is the measured result at i, y_i^{GP} is the GP mean result and n is the number of samples. The errors of LOO-CV for yield and antibacterial score are referred to as $\varepsilon_{LOO\text{-}CV,Y}$ and $\varepsilon_{LOO\text{-}CV,S}$.

8

(3) $\varepsilon = \frac{1}{n}\sum_{i=1}^{n}|\hat{y}_i - y_i^{GP}|$

7) Materials were synthesized at 6 chosen conditions with yield values of 0.6 g min^{-1} and antibacterial scores ranging from -0.6 to 3.8 mm to verify promising experimental conditions and to evaluate the model accuracy (i.e. "experimental evaluation"). Further, a limited set was further characterized with powder X-ray diffraction (XRD) and transmission electron microscopy (TEM). The errors of experimental evaluation for yield and antibacterial score are referred to as $\varepsilon_{exp,Y}$ and $\varepsilon_{exp,S}$.
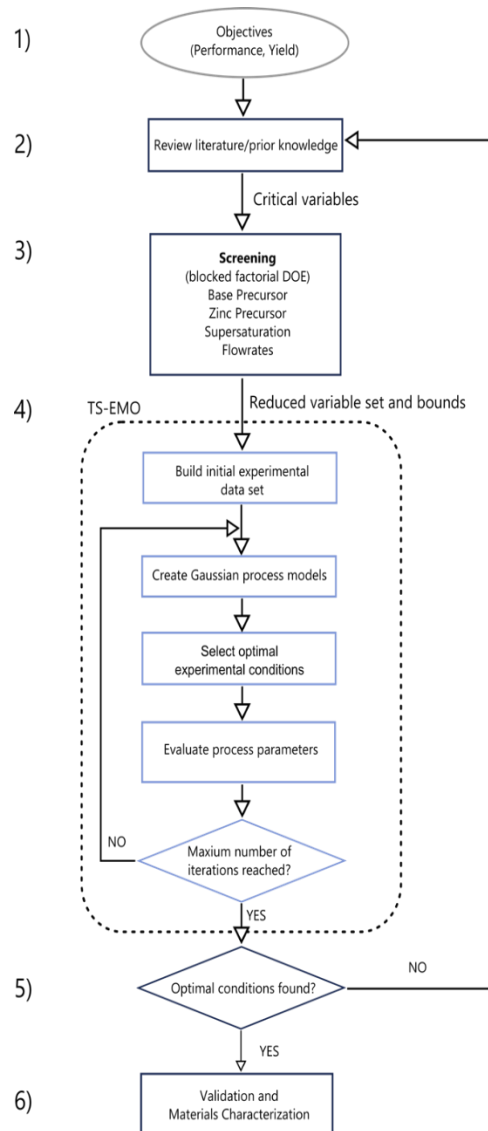

Figure 2. Schematic of the experimental design and optimization process.

2.4 Materials and reagents

Reagent grade $Zn(NO_3)_2\cdot6H_2O$, $Zn(SO_4)\cdot7H_2O$, $Zn(Cl)_2$, $Zn(CH_3CO_2)$, KOH ($\geq85\%$) and $NaOH$ ($\geq98\%$) were obtained from Sigma-Aldrich. Deionized water (Millipore) and ethanol (96% - Singapore Chemical Reagent Co.) were used as solvents. *E.Coli* ATCC 8739, nutrient broth (HiMedia-MM244) and nutrient agar (HiMedia-MM012) were supplied by Bio-Rev. Whatman No. 5 filter paper (VWR), Petri dishes (90 x 14 mm), sterile swabs, culture tubes and sodium chloride (NORMAPUR analytical reagent) were supplied by VWR.

2.5 Powder X-ray Diffraction

Suspensions were diluted in ethanol, drop-cast onto a non-reflective silicon wafer (100) and dried at 80 °C for 10 min. The powder x-ray diffraction pattern was collected with a Brucker D8 Advance Powder Diffractometer using Cu Kα radiation ($\lambda = 1.5418$ Å) at 40 kV from a 2θ of 3° to 70° with a step size of 0.02° and a scanning rate of 1.25° min^{-1}.

2.6 Transmission Electron Microscopy

Suspensions were diluted in ethanol, dropped on holey carbon 200 mesh copper TEM grids (InLab Supplies) and dried at ambient temperature. Images were taken with a JEOL 2100F FETEM at 200 kV.

3 RESULTS AND DISCUSSION

3.1 Optimization

From the 64 experiments performed (26 screening + 20 LHS + 18 TSEMO) an experimental Pareto front was resolved, ranging from antibacterial scores of -1.7 to 5.2 mm and yields of 0.56 to 0.71 g min^{-1} (shown in Figure 3a). If we take an antimicrobial score > 0 mm as a lower bound specification and target maximum yield, we find that the highest performing experimental condition produces ZnO with a score of 2.17 mm and a yield of 0.70 g min^{-1} (1.0 kg day^{-1}) in a single reactor.

Analyzing the set of conditions used (see Figure 3b) we see that the initial LHS training set provides a sufficient spread of testing conditions. During subsequent TSEMO iterations, the experimental conditions narrow to the set of optimal conditions. Interestingly, $C_{Zn,A}$ reaches a narrow region of optimal conditions after the first iteration, indicating that high concentrations can produce both high performance and high yield, which was not obvious from previous literature review. The results of each iteration are shown in Figure 3a.

The modelled Pareto front (i.e. the Pareto front of the GP model shown in Figure 3a) lies along the experimental Pareto front (i.e. the Pareto front of the experimental measurements). The modelled Pareto changes in shape as more data is added (seen in Figure 3c) showing an increase in accuracy with each iteration. The surprising steepness of the Pareto front and the narrow window of optimal processing conditions illustrate the sensitivity of this tradeoff to processing conditions and highlight the importance of finely controlled process parameters in the synthesis of nanomaterials.
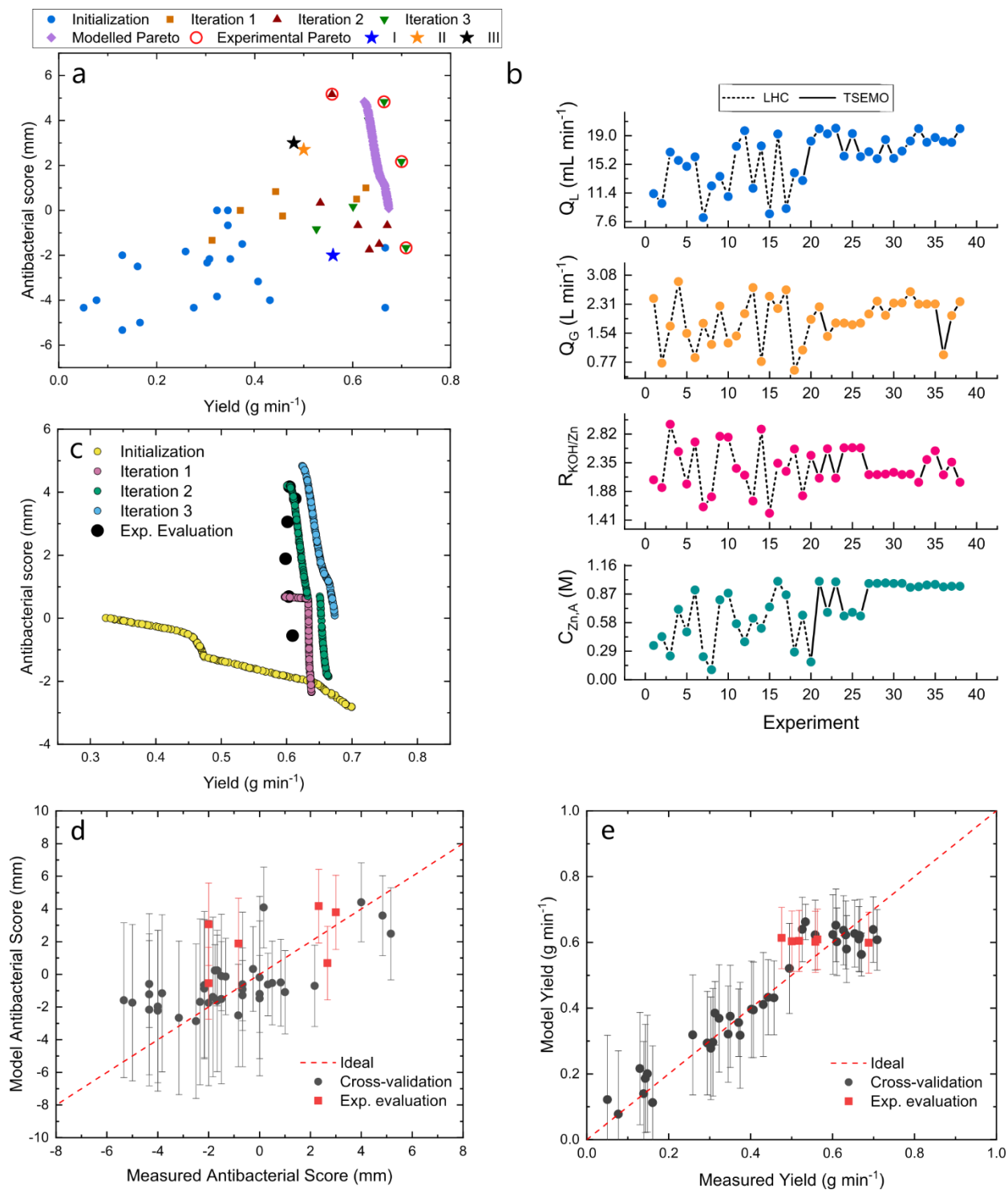
Figure 3. TSEMO optimization, crossvalidation and experimental evaluation results. a) Antibacterial score and yields for each experimental iteration and the final corresponding Pareto fronts (modeled and experimental) b) Corresponding experimental conditions, where Q_L is the total liquid flowrate, Q_G is the gas flowrate, $R_{KOH/Zn}$ is the molar ratio of KOH to Zn, and $C_{Zn,A}$ is the molar concentration of $Zn(NO_3)$ in reagent A. Data within the dashed lines are the

results of LHC initialization and data within the solid lines are results of TSEMO optimization c) Modelled Pareto fronts across different TSEMO iterations and model targets for experimental evaluation. d) Model antibacterial scores and e) yields compared with measured yields and antibacterial scores at the same conditions, where the red dashed line is the ideal fit (100%) and error bars are model 95% confidence intervals.

The results of model cross-validation and experimental evaluation are shown in Figure 3d and e, where the GP model predictions are compared with the respective measurements. The greater 95% confidence intervals of modelled antibacterial scores reflect the larger variance in experimentation. $\varepsilon_{exp,S}$ and $\varepsilon_{exp,Y}$ were 2.3 mm and 0.08 g min^{-1} respectively, while $\varepsilon_{LOO-CV,S}$ and $\varepsilon_{LOO-CV,Y}$ were 1.5 mm and 0.04 g min^{-1}. 89% of the cross-validation results lied within the 95% confidence interval of model predictions (seen in the error-bars of Figure 3d and e), indicating the accuracy of the model. Within the experimental evaluation, 4/6 of the yields and 5/6 of the antibacterial scores lied within the 95% confidence interval of model predictions.

Model variance is strongly influenced by the precision of experimental measurements. Antimicrobial tests had an average standard deviation of 1.03 mm (9.8% of the measurement range). This is close to $\varepsilon_{LOO-CV,S}$ and is likely due to variation in biological samples, filter papers and dosing of ZnO. Yield results had standard deviations of 0.04 g min^{-1} (5.8% of the measurement range), and is the same as $\varepsilon_{LOO-CV,Y}$, and may be a result of uneven sampling and loss of sample during purification.

Cross-validation errors were likely lower than the errors of experimental evaluations due to the increased sample size. Discrepancies between the TSEMO model predictions and experimental results may be a result of several factors. Model deviation likely arises from experimental noise as well as the DOE selected. TSEMO selects experimental points with dual objectives – increasing model accuracy ("exploration") and optimizing outputs ("exploitation") – which involves some sacrifice of global model accuracy. To increase the accuracy of the GP model, more data would be needed.

Furthermore, the larger deviations in predictions of antimicrobial activity may be attributed to the larger amounts of biological variation in samples, which in turn increase the error of the model. There may also be other variables that affect synthesis that are not accounted for in the model, for example, variations in the starting materials used across different batches from a single supplier and the microbiologist performing each test. Particle characteristics were also

13

not considered as model parameters within the study. The robustness of model predictions should be honed in the future by conducting larger numbers of experiments and including more variables.

In an extension to this study, pairing model predictions with output targets can guide further development and scale-up trials. For example, if we target an antibacterial score of ≥ 0 mm, the modelled Pareto front can be used to predict promising process conditions with 95% certainty. Processing tolerances could also be incorporated for sensitivity analysis. For example, although yields of up to 0.7 g min^{-1} can be achieved, the range of conditions that can achieve this may be very narrow, and a yield of 0.6 g min^{-1} may be a safer experimental target (see Figure 3c). The model yield can then be used to estimate the number of reactors needed for scale-up.

In further studies it is necessary to benchmark the GP model obtained from TSEMO to those using traditional chemical engineering methods, from simpler methods like empirical numerical models to the more complex, deterministic models that couple computational fluid dynamics, molecular dynamics and population balance models for crystal growth.

It is important to note the limitations of the specific methods used in our case study. Wet chemical synthesis and microreactors are not universally suitable for every new material. Process selection should initially be guided by practical knowledge; however, experimentalists still benefit from using efficient synthesis methods with well-defined engineering parameters early in the development. The design of experiment and/or statistical model used should also be tailored to the problem at hand. TSEMO is appropriate when multiple competing objectives exist, the variables used are continuous and experiments are expensive to evaluate. For problems in which objectives are noncompeting, variables are discrete or large datasets are readily obtained, the experimental problem may be significantly different and the present methodology can be extended through the selection of another DOE approach [60].

3.2   Synthesis and Characterization along the Pareto Front

Along the synthesis conditions of the Pareto front, Q_G and $R_{KOH:Zn}$ vary the most, from 2.0 to 2.6 L min^{-1} and from 2.03 to 2.40, (30% and 18% of their minimum values respectively). $R_{KOH:Zn}$ is correlated to increasing yield, possibly as a result of the decreased solubility of Zn^{2+} in more alkaline media, but may also lead to lower antibacterial scores. The gas flowrate strongly influences the hydrodynamics of the reactor. Increasing Q_G generally leads to higher shear rates and lower mixing times. Within the Pareto front conditions, the shear rates range from $3.2 \cdot 10^5$ to $4.8 \cdot 10^5$ s^{-1} and theoretical

energy dissipation rates range from 300 to 640 W/kg, corresponding to estimated characteristic micromixing times of 0.93 to 0.64 ms respectively. Calculated average reactor residence times varied from 13 to 29 ms, which are significantly greater than the characteristic micromixing times. Zinc reagent concentrations, ranging within 0.94-0.95 M were high compared to many published synthesis methods, which often use concentrations in the range of 0.01-0.1 M Zn^{2+} [46, 48, 51]. The liquid flowrate (Q_L) also occupied a narrow range close to its upper bound, 18-20 mL min^{-1}.

Materials synthesized with different antibacterial scores in experimental evaluation possessed significantly different morphologies and sizes, which are known correlators for antibacterial activity. Three distinct morphologies were observed – spheres, rods and stars – which are shown in Figure 4a-d and in Figure 3a (conditions I, II and III). Powder X-ray diffraction (XRD) of the structures confirmed that they possess the wurtzite ZnO structure (shown in Figure 4e). Across all conditions quasi-spherical particles ($\sim$17 ± 6 nm) are observed, and are the likely precursors for the larger structures (Figure 4a). In condition I, we produce large, star-like aggregates greater than 1 μm in diameter (Figure 4b). In condition II, we produce nanostars ($\sim$100 nm) and their aggregates, which were typically < 1 μm in size (Figure 4c). In condition III, we produce short rods with length of approximately 180 nm and an aspect ratio of 2 (Figure 4d). These structures have all been synthesized in previous studies through various methods (stars in references [48, 51], rods in references [46, 50] and quasi-spherical particles in references [35, 42], which allow us to make a clear mechanistic analysis of their formation mechanism.

Table 2. Selected synthesis conditions and material characteristics.

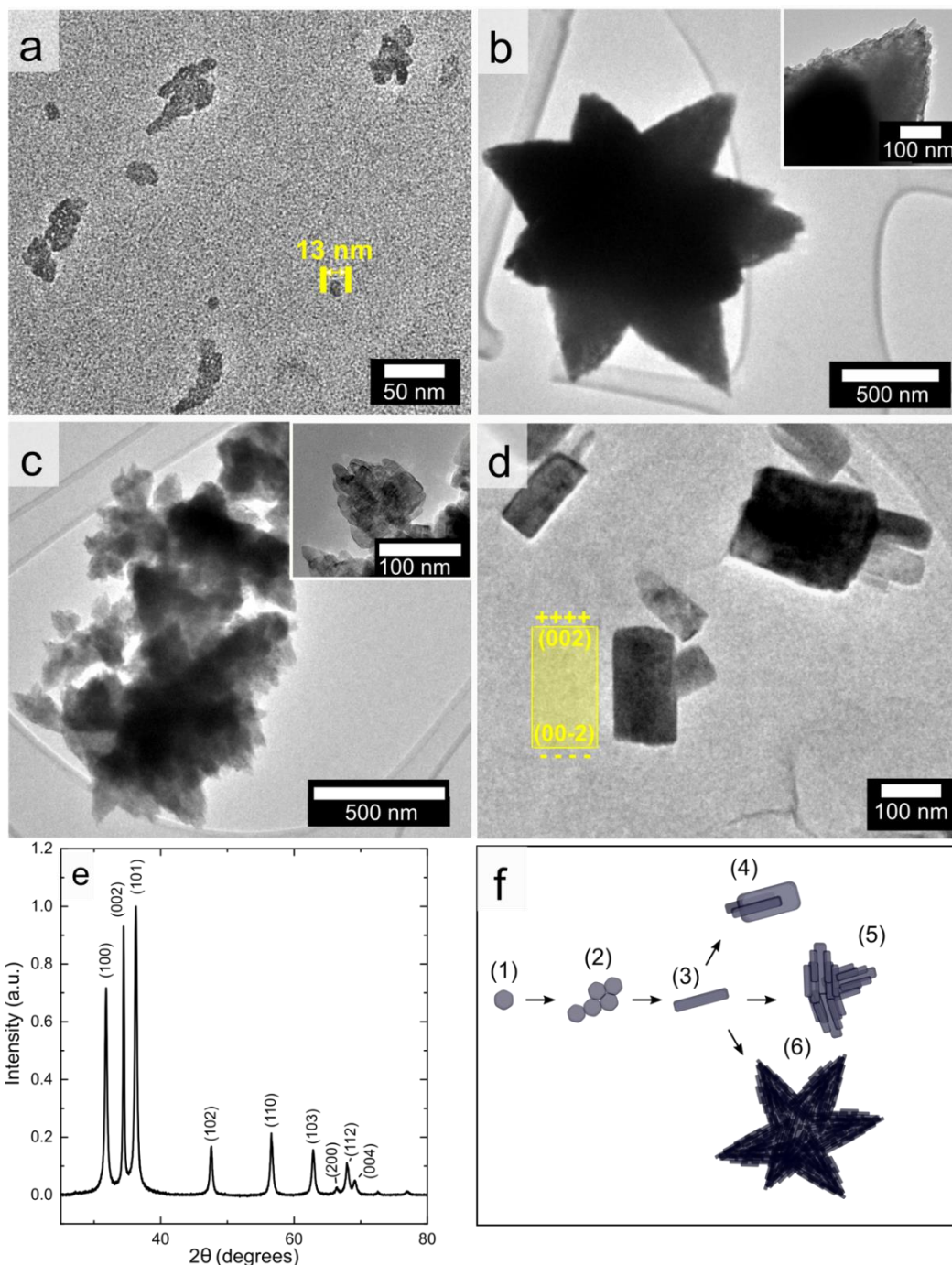| Condition	$C_{Zn,A}$ (M)	$R_{KOH:Zn}$	Q_G (L min^{-1})	Q_L (mL min^{-1})	Antimicrobial score (mm)	Shear rate (s^{-1})	Yield (g min^{-1})	Structure	Residence Time (ms)	Characteristic micromixing time (ms)
I	0.94	2.3	2.6	18.0	-2.0	$4.1\cdot10^{-5}$	0.56	Stars (>1 µm)	16	0.74
II	0.95	2.4	2.0	18.0	2.7	$2.9\cdot10^{-5}$	0.50	Nanostar (<1 µm)	19	1.0
III	0.95	2.0	1.9	18.0	3.0	$2.7\cdot10^{-5}$	0.48	Short rods (~180 nm)	19	1.1
I,II,III	-	-	-	-	-	-	-	Quasi-spherical (~ 17 nm)	-	-

Figure 4. Materials characterization of selected ZnO samples: TEM images of a) Precursor nanoparticles and their intermediate aggregates, b) micron-sized stars, c) nanostars and d) short rod assemblies. Inset in d) is a schematic indicating positions of the (002) and (00-2) planes and their charge signs on a representative crystal e) Representative XRD pattern, identified with the characteristic reflections of wurtzite ZnO at 2θ = 31.8°, 34.4°, 36.3°, 47.6°, 56.6°, 62.9°, 66.5°, 67.9° and 69.1° [61]. (f) Proposed structure formation pathway with steps (1) to (6) discussed in the text.

17

High shear reactors, such as the annular microreactor, rotor stator mixers [62], and other turbulent mixers [63] are known to influence the physical characteristics of nanomaterials, such as the particle size distribution, morphology and crystallinity, through a variety of mechanisms [8]. Shear stress is a key driving force for mixing by increasing bulk convective transport and molecular diffusion rates. Nanoparticle formation kinetics are often rapid, for example during nucleation in highly supersaturated precipitation, and necessitate fast mixing to obtain a homogeneous particle size and morphological distribution.

Furthermore, at high shear rates the dynamics of nanoparticles in fluid flow become sensitive to shear stress. Shear stress not only increases diffusion, which can accelerate aggregation, but can also stress particles, causing them to breakup [64-66], as in the case of graphene [22]. In the case of anisotropic particles, shear stress can influence the rotational diffusivity of particles, which in turn affects their alignment and formation of aggregate structures, affecting their size, morphology and crystallinity [67-69].

The formation of the different ZnO geometries is explained from the interplay of nucleation, growth, aggregation and hydrodynamics, and shown schematically in Figure 4f. Particle nucleation rates are governed by the drive to lower free energy - in the reactive precipitation of ZnO, this is driven by the supersaturation of Zn^{2+} and concentration of hydroxyl ions. Our use of highly concentrated solutions paired with fast mixing effectively results in a LaMer-type precipitation [70, 71], in which nucleation and growth are segregated, and result in the formation of the observed, smaller quasi-spherical particles, which are the precursors for later growth and aggregation (step 1 in Figure 4f). The high shear rates and sub-millisecond characteristic micromixing times achieved in AMS are essential for achieving this crystallization pathway.

Driven to lower their surface energy, the nanoparticles then crystallize *via* oriented attachment (steps 2-3 in Figure 4f), which is driven by surface reduction [42], direction specific interactions [56] and surface active species [54]. The concentration of hydroxyl ions is known to play a key role in the crystallization of ZnO nanostructures, possibly due variations in their interactions with specific ZnO crystal faces, where increasing hydroxyl concentration increases the anisotropy of growth along the <002> directions [46, 50, 51]. High shear rates also influence the oriented attachment of anisotropic nanoparticles in AMS, as has been observed in previous studies with layered double hydroxides [15].

18

At lower hydroxyl concentrations and low shear rates (condition III), anisotropic particles attach to form short rods (step 4 in Figure 4f). With increasing hydroxyl concentrations (conditions I and II, corresponding to steps 6 and 5 respectively in Figure 4f), more anisotropic structures form, and higher shear rates accelerate their oriented attachment and aggregation. The star shape arises from the branching of rods from a central origin. Condition II has a higher KOH:Zn^{2+} ratio but a lower shear rate than Condition II, likely explaining in the difference in size of the star-shaped structures.

The antibacterial effects of ZnO stem from a collection of physical and chemical interactions with *E.Coli*. ZnO surface defects catalyze the production of radical oxygenated species (ROS) and H_2O_2 that damage the cellular envelope and components, solubilized Zn^{2+} enters cells and disrupts internal processes, and ZnO nanostructures electrostatically interact with cell membranes, causing them to rupture [45, 72]. In the antibacterial test used, diffusivity across the agar surface is also an important factor. In general, smaller particle sizes will increase the concentration of surface defects, speed of Zn^{2+} dissolution, local electric field strength, and particle diffusivity. Therefore, the ~17 nm precursor particles are likely a dominating source of the antibacterial activity. The shapes and sizes of particle assemblies then determine the surface area-to-volume ratio, diffusivity and resulting efficiency of the material. Smaller and less dense structures, such as the short rods and nanostars possess both higher surface-area-to-volume ratios and higher diffusivity, resulting in their higher antibacterial activity. With higher relative surface areas, smaller particles possess an increased number of active surface sites for the catalytic production of ROS. Smaller particles will also be more sensitive to Brownian forces, and will thus diffuse more quickly in liquid mediums to interact with a greater number of bacteria. The electrostatic field is also enhanced by morphology; for example, the internal electric field of ZnO is generated from the positive charge (terminal Zn^{2+}) of the (002) plane and the negative charge (terminal O^{2-}) of the (00-2) plane, respectively (inset, Figure 4d); it is thus observed that the antibacterial activity of the short rods (3.0 mm, Table 2) is higher than those of the nanostars (2.7 mm, Table 2) and large stars (-2.0 mm, Table 2).

It is important to note that, in this study, only the antimicrobial performance and yield were modelled as functions of synthesis conditions. In comparison to typical materials science studies, the amount of physical materials characterization was purposefully light; TEM and XRD were only performed on select samples on the Pareto front. While this produces less "fundamental" knowledge initially, it identified important relationships between the materials and processing conditions that can be further studied. Sufficient data to correlate particle characteristics like size and

morphology with yield in annular microreactor synthesis were not collected in this analysis. This is the scope of future studies.

Particle characteristics are not considered by the TSEMO modelling approach, as the study's objectives are only to target high antimicrobial activity and high yield. Inclusion of data on particle characteristics may be essential to improve the model and further examine why deviations occur. For such a specific study on particle characteristics, one would need to modify the TSEMO algorithm to accept particle attributes as outputs, and select objective targets related to those. The accuracy of modelled predictions would then also depend on the accuracy of particle measurements and the experimentalist's ability to control synthesis parameters.

For example, to examine the trade-off between yield and particle morphology, quantitative measurements of the particle shapes must be taken from each experiment. Both yield and particle data would then be taken as an input to the algorithm, which would then output a model for the relationship between the two objectives, in addition to suggestions for future experiments that could increase the accuracy of the model and optimize yield and particle size with respect to the desired targets.

3.3 Development Acceleration and Scalability Analysis

Compared to conventional DOE techniques for multi-factor problems, the machine-learning approach has significant advantages. Many experimenters use an "Edisonian" or empirical screening approach where only one factor is varied in an experimental run. This is inefficient, confounds the roles of different factors, and can lead to misidentification of maxima [12]. Factorial designs, which primarily focus on exploring the experimental parameter space, are better able to establish correlations and reduce confounding, but the number of experiments increases exponentially with the number of factors and levels. With two- or three-level factorial designs, non-monotonic relationships are also difficult to resolve. Fractional or "blocked" factorial designs can reduce this issue if some relationships are found to be insignificant, though at the risk of confounding and reduced resolution. For this reason, we only used a blocked factorial design for an initial screen to reduce the number of potentially redundant variables and identify ranges for conditions to optimize.

Response surface methodologies like TSEMO are better suited for multivariable optimization problems [73]. Surrogate-based optimization using GPs is well-suited for multivariable optimization for moderate input dimensions since GPs

are multivariable regression models. For example, in the original algorithm paper [29] it is shown that the algorithm shows good performance for up to 8 inputs. Randomized selection of the initial training dataset provides a better distribution of experimental points with fewer experiments and can identify non-monotonic relationships. Then, sequential optimization algorithms (gradient-based or otherwise) compromise exploration of search space and exploitation of promising areas to more efficiently lead to optimal conditions [60, 74].

For the optimization of four continuous variables, as seen in Figure 5a and b, a 3-level factorial design, requiring $3^4 = 81$ experiments (20.25 days), gives a sparse set of experimental conditions, which would not identify the optimal conditions. A 4-level factorial design, requiring $4^4 = 256$ experiments (64 days) would give a better distribution of conditions that may contain the optimum, but would sacrifice resolution within the optimal region. Our approach requires 64 experiments (16 days) to both identify optimal conditions and the Pareto front, significantly accelerating the development process.

Although high-throughput disk-diffusion testing increases uncertainty in test results, it reduces the experimental time needed to characterize material. Quantitative analysis *via* counting of colony forming units significantly increases experimental time because it requires up to three days of culturing per batch and significantly more labor due to the increased cell culturing and colony counting [75]. The cumulative experimental times for each DOE method and test method for gram scale optimization are shown in Figure 5c.
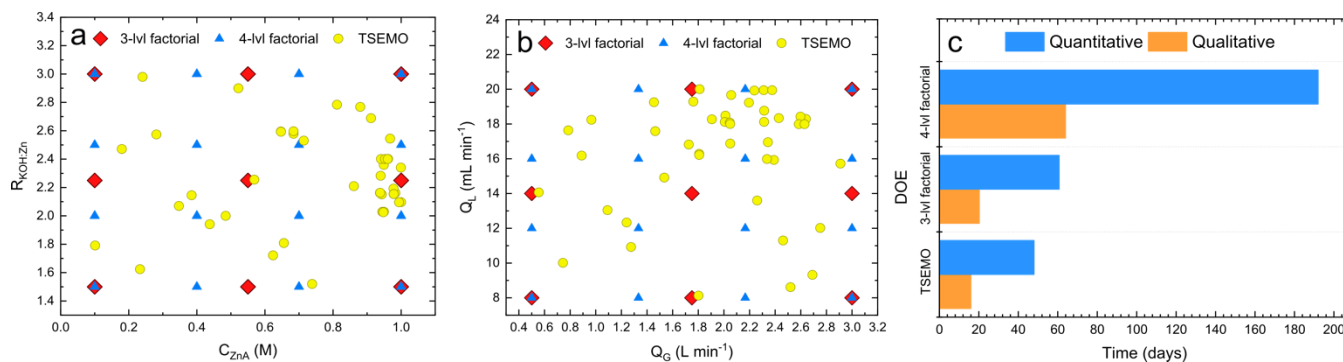

Figure 5. Comparison of selected conditions across (a) $R_{KOH:Zn}$ and $C_{Zn,A}$ and (b) Q_L and Q_G from factorial designs and TSEMO (using the LHS initial dataset). (c) Comparison of cumulative experimental time between different DOEs and antibacterial test methods.

Compared to conventional laboratory synthesis techniques, AMS of antibacterial ZnO is significantly more efficient. The space-time yield, reported here as the yield divided by solvent volume, is 62.4 kg day^{-1} m^{-3}, which is $10^2 - 10^5$ times greater than other reported methods, shown in Figure 6a, and described in Table 3. Operating at room temperature reduces power consumption, compared to reported continuous methods and decreases process hazards. Using water as a solvent also reduces process hazards and material costs. Process efficiency could be further increased by the removal of byproduct potassium nitrate (which can be resold for a range of industrial uses) and recycling of solvent, though further technoeconomic analysis would also be necessary to make this case.

Table 3. Description of the reported reactors used for batch and continuous nanoparticle ZnO synthesis.

Reference	Reactor description
Liu *et al.,* 2004 [46]	Covered plastic container 250 mL in volume under constant stirring. Reactor geometry and agitation method are unreported.
Sondergaard *et al.,* 2011 [51]	Specially designed supercritical fluid synthesis apparatus. Geometry is unreported.
Oliveira *et al.*, 2003 [48]	Double walled water-jacketed hemispheric reactor, 1.5 L capacity with four Teflon baffles, 45 deg tilted blade propellor @ 500 rpm. Impeller blade dimensions and immersion depth are unreported.
Sue *et al.*, 2003 [52]	T mixer in an elbow configuration, consisting of a 2.38 mm inner diameter nozzle for a $Zn(NO_3)_2$/KOH sol, a 2 mm ID nozzle for supercritical water, and a 2 mm inner diameter reaction tube (0.51 cm^3 volume).
Wu *et al.*, 2007 [35]	Vigorously stirred flask with refluxing. Geometry or dimensions are unreported.

Projected scaling up of AMS of ZnO *via* number-up presents significant advantages, primarily from the reduction of complexity. This is illustrated in a comparison of hypothetical scaling scenarios with stirred tank reactors (STRs), the most common reactor for bottom-up wet synthesis, as shown in Figure 6b and Table 4. In g day^{-1} synthesis, AMS and stirred tank reactors require the optimization of the same number of variables (7). When shifting to kg day^{-1} synthesis, it is necessary to define engineering and scaling parameters in a STR, which is typically a heuristic and experimental process if they have not been defined through extensive simulations. For many materials produced in the typical magnetically stirred flask, these parameters are undefined. Dimensionless parameters, such as Reynolds number (Re),

Nusselt number (Nu) and Damköhler number (Da) describe the dynamics of mass transfer, heat transfer and reaction kinetics, which affect material formation and should stay as constant as possible to retain process consistency during scale-up [76]. These parameters are functions of the physical geometry and operating conditions of each unit operation, such as the reactor size and agitator method. In our scenario, we have considered six additional variables, shown in Table 4. In this case study, AMS was able to achieve kg day^{-1} scale production rates using a single reactor stage, in which engineering parameters, such as the mixing rate and reactor geometry are already well defined. Temperature regulation in the single reactor is not necessary because the reaction is not strongly exothermic, and the compressed dried air stream is a sufficient temperature control agent.
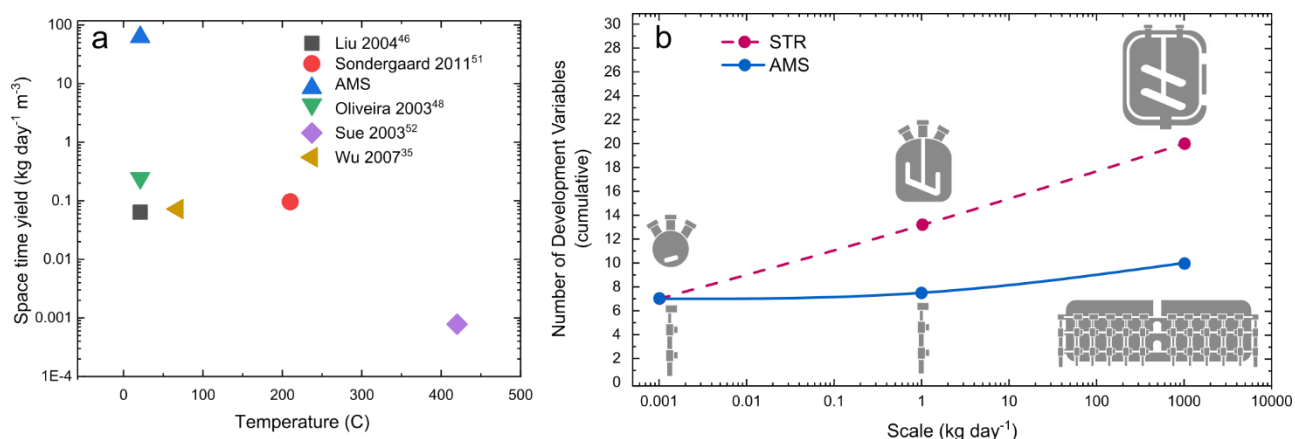

Figure 6. Comparison of AMS with other synthesis methods: (a) space time yields of different reported techniques for nano-ZnO synthesis vs synthesis temperature, (b) scale-up complexity in terms of development dimensions for the scale-up of stirred tank reactors and numbering-up of AMS. Lines are added to guide the eye.

When translating stirred tank reactors to the ton day^{-1} scale, the reactor geometry, agitation and maintenance (cleanout) parameters must be defined again, although the previous identification of engineering parameters from the kg day^{-1} scale reduces the difficulty [76-79]. On the other hand, AMS scales to ton day^{-1} by simply multiplying the number of reactors, which can be achieved using proper manifolding techniques (for which established design rules are known) and machining tolerances [20, 80]. This allows precise conservation of engineering parameters from the g and kg day^{-1} scale, and only requires the design of temperature control and optimization of a maintenance schedule. In total, for the hypothetical scale-up scenario, scaling AMS involves 10 dimensions compared to 20 for stirred tank reactors, halving the complexity. AMS may also be scaled *via* increase of tubing diameter, scaling the flowrates and tubing length to conserve shear rates, micromixing times and residence times. Targeting the correct flowrates and tube dimensions for parameter conservation may be done by hydrodynamic modelling or experimentally.

Table 4. Potential variables in a scale-up scenario, comparing batch stirred reactors and AMS.

Scale	Variables	
	Batch Stirred Reactor	Annular Microreactor
g	Solvent (1)	Solvent (1)
	Reagents (2)	Reagents (2)
	Reagent Concentrations (2)	Reagent Concentrations (2)
	Reaction time (1)	Flowrates (2)
	Stirring rate (1)	
kg	Reactor volume (1)	-
	Reactor shape (1)	
	Stirrer type (1)	
	Reaction time (1)	
	Stirring speed (1)	
	Heat power (1)	
ton	Reactor volume (1)	Manifold geometry (1)
	Reactor shape (1)	Cleanout frequency (1)
	Stirrer type (1)	Heat power (1)
	Reaction time (1)	
	Stirring speed (1)	
	Heat power (1)	
	Cleanout frequency (1)	
Total Dimensions	20	10

The costs of scaling may also be reduced through a number-up strategy. In numbering-up, a single reactor is scaled by increasing the number of reactors and operating them in parallel. This can be achieved through a range of techniques, most commonly with the use of a single pump and distribution manifolds [20]. Conventional stirred tank reactor costs scale nearly linearly with reactor volume [81] and are sensitive to supplier lead times and material availability. If single reactors can be mass produced with precision injection moulding processes or additive manufacturing, reactor costs

may decrease per unit capacity. Furthermore, numbering-up using prefabricated modular components is well suited for distributed chemical processes and has an accelerated learning ratio [82], which could further lower costs in some business models.

Numbering-up of AMS to the ton scale is another important milestone to be achieved, which requires precision manufacturing and manifold design, and is the topic of current research. Additive manufacturing and injection molding are potentially viable techniques for mass production of modular annular microreactor components. The use of such equipment can enable rapid reactor prototyping, standardize development practices in different laboratories, and simplify distribution.

4   CONCLUSIONS

In summary, the pairing of annular microreactor synthesis, the multiobjective optimization algorithm TSEMO and highthroughput testing for the development of antibacterial ZnO has yielded three significant results. An optimized process for 1 kg per day production of a material with activity comparable to a commercially available antimicrobial and conventionally synthesized nano-ZnO was developed in less than 100 experiments. A brief analysis of the materials synthesized in these trials suggested that nanostar and nanorod morphologies may emerge from the assembly of nanoparticle precursors, and that the interplay of surface area, anisotropy and particle size influence antibacterial activity. Finally, a scalablility assessment was conducted, and showed how scaling-up of AMS *via* numbering-up may reduce the complexity of scaling. This study also opens new grounds for further improvements in the area. Validation should be performed with traditional chemical engineering techniques for crystal growth simulation and process scale-up. The accuracies of models produced using TSEMO should also be improved, particularly in regions of high yields (> 0.5 g min^{-1}) and where there is a steep Pareto front. Computational methods for the automated screening of literature [83] and simulation of structures can accelerate the initial efforts of process design. The same methodology could also be applied to downstream processes, particularly in purification and product formulation, where multi-step optimization methods may be required.

5   ACKNOWLEDGMENTS

6   DECLARATION OF COMPETING INTEREST

NJ, MK and AAL are founders of Accelerated Materials Ltd (acceleratedmaterials.co.uk), which commercializes the technology of nanomaterials synthesis in coaxial co-flow reactors.

7   REFERENCES

[1] M.L. Green, C.L. Choi, J.R. Hattrick-Simpers, A.M. Joshi, I. Takeuchi, S.C. Barron, E. Campo, T. Chiang, S. Empedocles, J.M. Gregoire, A.G. Kusne, J. Martin, A. Mehta, K. Persson, Z. Trautt, J. Van Duren, A. Zakutayev, Fulfilling the promise of the materials genome initiative with high-throughput experimental methodologies, Appl Phys Rev 4 (2017) 011105.

[2] H. Chraye, An ecosystem to accelerate the uptake of innovation in materials technology, European Commission, Luxembourg, 2017.

[3] J.J. de Pablo, N.E. Jackson, M.A. Webb, L.Q. Chen, J.E. Moore, D. Morgan, R. Jacobs, T. Pollock, D.G. Schlom, E.S. Toberer, J. Analytis, I. Dabo, D.M. DeLongchamp, G.A. Fiete, G.M. Grason, G. Hautier, Y.F. Mo, K. Rajan, E.J. Reed, E. Rodriguez, V. Stevanovic, J. Suntivich, K. Thornton, J.C. Zhao, New frontiers for the materials genome initiative, Npj Comput Mater 5 (2019) 41.

[4] A matter of scale, Nat Nanotech 11 (2016) 733-733.

[5] R. Paliwal, R.J. Babu, S. Palakurthi, Nanomedicine Scale-up Technologies: Feasibilities and Challenges, Aaps Pharmscitech 15 (2014) 1527-1534.

[6] T. Tsuzuki, Commercial scale production of inorganic nanoparticles, Int J Nanotechnol 6 (2009) 567-578.

[7] A.E.D.M. van der Heijden, Developments and challenges in the manufacturing, characterization and scale-up of energetic nanomaterials - A review, Chem Eng J 350 (2018) 939-948.

[8] N. Jose, A. Lapkin, Chapter 2 - Influence of Hydrodynamics on Wet Syntheses of Nanomaterials, in: V.A. Sadykov (Ed.) Advanced Nanomaterials for Catalysis and Energy, Elsevier, 2019, pp. 29-59.

[9] J.P. Correa-Baena, K. Hippalgaonkar, J. van Duren, S. Jaffer, V.R. Chandrasekhar, V. Stevanovic, C. Wadia, S. Guha, T. Buonassisi, Accelerating Materials Development via Automation, Machine Learning, and High-Performance Computing, Joule 2 (2018) 1410-1420.

[10] J. Harmsen, Chapter 9 - Industrial Scale-Up Cases, in: J. Harmsen (Ed.) Industrial Process Scale-up, Elsevier Amsterdam, 2013, pp. 99-113.

[11] J. Schmidt, M.R.G. Marques, S. Botti, M.A.L. Marques, Recent advances and applications of machine learning in solid-state materials science, Npj Comput Mater 5 (2019) 83.

[12] B. Cao, L.A. Adutwum, A.O. Oliynyk, E.J. Luber, B.C. Olsen, A. Mar, J.M. Buriak, How To Optimize Materials and Devices via Design of Experiments and Machine Learning: Demonstration Using Organic Photovoltaics, ACS Nano 12 (2018) 7434-7444.

[13] J.N. Kumar, Q.X. Li, K.Y.T. Tang, T. Buonassisi, A.L. Gonzalez-Oyarce, J. Ye, Machine learning enables polymer cloud-point engineering via inverse design, Npj Comput Mater 5 (2019) 73.

[14] J. Harmsen, Chapter 7 - Scale up of unit operations, in: J. Harmsen (Ed.) Industrial Process Scale-up, Elsevier, Amsterdam, 2013, pp. 59-71.

[15] N.A. Jose, H.C. Zeng, A.A. Lapkin, Hydrodynamic assembly of two-dimensional layered double hydroxide nanostructures, Nat Commun 9 (2018) 4913.

[16] S.D. Pask, Z.Z. Cai, H. Mack, L. Marc, O. Nuyken, The Spinning Disk Reactor for Polymers and Nanoparticles, Macromol React Eng 7 (2013) 98-106.

[17] Q. Wang, S.V.Y. Tang, E. Lester, D. O'Hare, Synthesis of ultrafine layered double hydroxide (LDHs) nanoplates using a continuous-flow hydrothermal reactor, Nanoscale 5 (2013) 114-117.

[18] K.J. Wu, G.M.D. Bohan, L. Torrente-Murciano, Synthesis of narrow sized silver nanoparticles in the absence of capping ligands in helical microreactors, React Chem Eng 2 (2017) 116-128.

[19] L. Falk, J.M. Commenge, Performance comparison of micromixers, Chem Eng Sci 65 (2010) 405-411.

[20] Q.Y. Shen, C. Zhang, M.F. Tahir, S.K. Jiang, C.Y. Zhu, Y.G. Ma, T.T. Fu, Numbering-up strategies of micro-chemical process: Uniformity of distribution of multiphase flow in parallel microchannels, Chem. Eng. Process. 132 (2018) 148-159.

[21] P. Yaseneva, N. An, M. Finn, N. Tiedemann, N. Jose, A. Voutchkova-Kostal, A. Lapkin, Continuous synthesis of doped layered double hydroxides in a meso-scale flow reactor, Chem Eng J 360 (2019) 190-199.

[22] K.R. Paton, E. Varrla, C. Backes, R.J. Smith, U. Khan, A. O'Neill, C. Boland, M. Lotya, O.M. Istrate, P. King, T. Higgins, S. Barwich, P. May, P. Puczkarski, I. Ahmed, M. Moebius, H. Pettersson, E. Long, J. Coelho, S.E. O'Brien, E.K. McGuire, B.M. Sanchez, G.S. Duesberg, N. McEvoy, T.J. Pennycook, C. Downing, A. Crossley, V. Nicolosi, J.N. Coleman, Scalable production of large quantities of defect-free few-layer graphene by shear exfoliation in liquids, Nat Mater 13 (2014) 624-630.

[23] L. Torrente-Murciano, A.A. Lapkin, D. Chadwick, Synthesis of high aspect ratio titanate nanotubes, Journal of Materials Chemistry 20 (2010) 6484-6489.

[24] C.H.S. Chakra, V. Rajendar, K.V. Rao, M. Kumar, Enhanced antimicrobial and anticancer properties of ZnO and TiO2 nanocomposites, 3 Biotech 7 (2017) 89.

[25] A. Krol, P. Pomastowski, K. Rafinska, V. Railean-Plugaru, B. Buszewski, Zinc oxide nanoparticles: Synthesis, antiseptic activity and toxicity mechanism, Adv. Colloid. Interfac. 249 (2017) 37-52.

[26] O. Zakharova, E. Kolesnikov, E. Vishnyakova, N. Strekalova, A. Gusev, Antibacterial activity of ZnO nanoparticles: dependence on particle size, dispersion media and storage time, IOP C Ser. Earth Env. 226 (2019) 0126062.

[27] N.H. Harun, R.B. S.M.N Mydin, S. Sreekantan, K.A. Saharudin, N. Basiron, F. Radhi, A. Seeni, Shape-Dependent Antibacterial Activity against Escherichia coli of Zinc Oxide Nanoparticles, JBCS 3 (2019) 35-38.

[28] N.A. Jose, H.C. Zeng, A.A. Lapkin, Scalable and precise synthesis of two-dimensional metal organic framework nanosheets in a high shear annular microreactor, Chem Eng J 388 (2020) 124133.

[29] E. Bradford, A. Schweidtmann, A. Lapkin, Efficient multiobjective optimization employing Gaussian processes, spectral sampling and a genetic algorithm, J Glob Optim 71 (2018) 407-438.

[30] A.C. Schweidtmann, A.; Holmes, N.; Bradford, E.; Bourne, R.; Lapkin, A., Machine learning meets continuous flow chemistry: Automated optimization towards the Pareto front of multiple objectives, Chem Eng J 352 (2018) 277-282.

[31] A.D. Clayton, A.M. Schweidtmann, G. Clemens, J.A. Manson, C.J. Taylor, C.G. Nino, T.W. Chamberlain, N. Kapur, A.J. Blacker, A.A. Lapkin, R.A. Bourne, Automated self-optimisation of multi-step reaction and separation processes using machine learning, Chem Eng J 384 (2020) 123340.

[32] Y. Han, H. Kanno, Y.J. Ahn, N. Shikazono, Measurement of liquid film thickness in micro tube annular flow, Int J Multiphas Flow 73 (2015) 264-274.

[33] J. Baldyga, J.R. Bourne, Simplification of Micromixing Calculations .1. Derivation and Application of New Model, Chem Eng J Bioch Eng 42 (1989) 83-92.

[34] J. Hudzicki, Kirby-Bauer disk diffusion susceptibility test protocol, American Society for Microbiology Conference for Undergraduate Educators, American Society for Microbiology, 2009.

[35] L.Y.L. Wu, A.I.Y. Tok, F.Y.C. Boey, X.T. Zeng, X.H. Zhang, Chemical synthesis of ZnO nanocrystals, Ieee T Nanotechnol 6 (2007) 497-503.

[36] B. Avci, Y. Caglar, M. Caglar, Controlling of surface morphology of ZnO nanopowders via precursor material and Al doping, Mat Sci Semicon Proc 99 (2019) 149-158.

[37] D. Banerjee, A.K. Kar, Effect of hydroxide ion concentration on the evolution of nanostructures and structure correlated luminescence of ZnO nanopowders, Opt Mater 89 (2019) 430-440.

[38] R. Chaudhari, D. Landge, C.J. Bhongale, A new insight into the adsorption-dissolution growth mechanism of zinc oxide hollow hexagonal nanotowers, RSC Advances 9 (2019) 20728-20732.

[39] B. Cheng, E.T. Samulski, Hydrothermal synthesis of one-dimensional ZnO nanostructures with different aspect ratios, Chem. Commun. 8 (2004) 986-987.

[40] F. Delgado-Licona, E.A. López-Guajardo, J. González-García, K.D.P. Nigam, A. Montesinos-Castellanos, Intensified tailoring of ZnO particles in a continuous flow reactor via hydrothermal synthesis, Chem Eng J 396 (2020) 125281.

[41] M. Distaso, M. Mackovic, E. Spiecker, W. Peukert, Early Stages of Oriented Attachment: Formation of Twin ZnO Nanorods under Microwave Irradiation, Chem Eur J 18 (2012) 13265-13268.

[42] D. Hapiuk, B. Masenelli, K. Masenelli-Varlot, D. Tainoff, O. Boisron, C. Albin, P. Melinon, Oriented Attachment of ZnO Nanocrystals, J Phys Chem C 117 (2013) 10220-10227.

[43] E. Hosono, S. Fujihara, T. Kimura, H. Imai, Non-Basic Solution Routes to Prepare ZnO Nanoparticles, J. Sol-Gel Sci. Techn. 29 (2004) 71-79.

[44] H.W. Kang, J. Leem, S.Y. Yoon, H.J. Sung, Continuous synthesis of zinc oxide nanoparticles in a microfluidic system for photovoltaic application, Nanoscale 6 (2014) 2840-2846.

[45] R. Kumar, A. Umar, G. Kumar, H.S. Nalwa, Antimicrobial properties of ZnO nanomaterials: A review, Ceram Int 43 (2017) 3940-3961.

[46] B. Liu, H.C. Zeng, Room temperature solution synthesis of monodispersed single-crystalline ZnO nanorods and derived hierarchical nanostructures, Langmuir 20 (2004) 4196-4204.

[47] M. Mrad, B. Chouchene, T. Ben Chaabane, Effects of Zinc Precursor, Basicity and Temperature on the Aqueous Synthesis of ZnO Nanocrystals, S Afr J Chem-S-Afr T 71 (2018) 103-110.

[48] A.P.A. Oliveira, J.F. Hochepied, F. Grillon, M.H. Berger, Controlled precipitation of zinc oxide particles at room temperature, Chem Mater 15 (2003) 3202-3207.

[49] C. Pacholski, A. Kornowski, H. Weller, Self-assembly of ZnO: From nanodots to nanorods., Angew. Chem. Int. Ed. 41 (2002) 1188-1191.

[50] R. Raji, K.G. Gopchandran, ZnO nanostructures with tunable visible luminescence: Effects of kinetics of chemical reduction and annealing, J. Sci-Adv. Mater. Dev. 2 (2017) 51-58.

[51] M. Sondergaard, E.D. Bojesen, M. Christensen, B.B. Iversen, Size and Morphology Dependence of ZnO Nanoparticles Synthesized by a Fast Continuous Flow Hydrothermal Method, Cryst Growth Des 11 (2011) 4027-4033.

[52] K. Sue, K. Murata, K. Kimura, K. Arai, Continuous synthesis of zinc oxide nanoparticles in supercritical water, Green Chem 5 (2003) 659-662.

[53] P. Wainer, O. Kendall, A. Lamb, S.J. Barrow, A. Tricoli, D.E. Gomez, J. van Embden, E. Della Gaspera, Continuous Growth Synthesis of Zinc Oxide Nanocrystals with Tunable Size and Doping, Chem Mater 31 (2019) 9604-9613.

[54] J. Wang, X. Li, C.J. Teng, Y. Xia, J.L. Xu, D. Xie, L. Xiang, S. Komarneni, Ligand-directed rapid formation of ultralong ZnO nanowires by oriented attachment for UV photodetectors, J Mater Chem C 4 (2016) 5755-5765.

[55] Z.H. Zhang, M.H. Lu, H.R. Xu, W.S. Chin, Shape-controlled synthesis of zinc oxide: A simple method for the preparation of metal oxide nanocrystals in non-aqueous medium, Chem. Eur. J. 13 (2007) 632-638.

[56] X. Zhang, Z. Shen, J. Liu, S.N. Kerisit, M.E. Bowden, M.L. Sushko, J.J. De Yoreo, K.M. Rosso, Direction-specific interaction forces underlying zinc oxide crystal growth by oriented attachment, Nat Commun 8 (2017) 835.

[57] A. Ziashahabi, R. Poursalehi, N. Naseri, Formation mechanism of bead-chain-like ZnO nanostructures from oriented attachment of Zn/ZnO nanocomposites prepared via DC arc discharge in liquid, Mat Sci Semicon Proc 72 (2017) 128-133.

[58] M. Stein, Large Sample Properties of Simulations Using Latin Hypercube Sampling, Technometrics 29 (1987) 143-151.

[59] M. Stone, Cross-Validatory Choice and Assessment of Statistical Predictions, J R Stat Soc B 36 (1974) 111-147.

[60] A. Schweidtmann, D. Bongartz, D. Grothe, T. Kerkenhoff, X. Lin, J. Najman, A. Mitsos, Global Optimization of Gaussian processes, arXiv e-prints (2020) 2005.10902.

[61] K. Kihara, G. Donnay, Anharmonic thermal vibrations in ZnO, Can. Mineral 23 (1985) 647-654.

[62] M. Jasinska, J. Baldyga, M. Cooke, A. Kowalski, Application of test reactions to study micromixing in the rotor-stator mixer (test reactions for rotor-stator mixer), Appl Therm Eng 57 (2013) 172-179.

[63] J.L. Zhang, S.Q. Xu, W. Li, High shear mixers: A review of typical applications and studies on power draw, flow pattern, energy dissipation and transfer properties, Chemical Engineering and Processing-Process Intensification 57-58 (2012) 25-41.

[64] A. Zaccone, M. Soos, M. Lattuada, H. Wu, M.U. Babler, M. Morbidelli, Breakup of dense colloidal aggregates under hydrodynamic stresses, Physical Review E 79 (2009).

[65] A. Zaccone, D. Gentili, H. Wu, M. Morbidelli, Shear-induced reaction-limited aggregation kinetics of Brownian particles at arbitrary concentrations, Journal of Chemical Physics 132 (2010).

[66] N.D. Vassileva, D. van den Ende, F. Mugele, J. Mellema, Restructuring and break-up of two-dimensional aggregates in shear flow, Langmuir 22 (2006) 4959-4967.

[67] J. Vermant, M.J. Solomon, Flow-induced structure in colloidal suspensions, J Phys-Condens Mat 17 (2005) R187-R216.

[68] P. Szymczak, M. Cieplak, Proteins in a shear flow, J Chem Phys 127 (2007) 155106.

[69] R.C. Sonntag, W.B. Russel, Structure and Breakup of Flocs Subjected to Fluid Stresses .1. Shear Experiments, Journal of Colloid and Interface Science 113 (1986) 399-413.

[70] G.M. Pound, V.K. Lamer, Kinetics of Crystalline Nucleus Formation in Supercooled Liquid Tin, J Am Chem Soc 74 (1952) 2323-2332.

[71] V.K. Lamer, R.H. Dinegar, Theory, Production and Mechanism of Formation of Monodispersed Hydrosols, J Am Chem Soc 72 (1950) 4847-4854.

[72] T.B. Rawal, A. Ozcan, S.H. Liu, S.V. Pingali, O. Akbilgic, L. Tetard, H. O'Neill, S. Santra, L. Petridis, Interaction of Zinc Oxide Nanoparticles with Water: Implications for Catalytic Activity, Acs Appl Nano Mater 2 (2019) 4257-4266.

[73] D.C. Montgomery, Chapter 11 - Response surface methods and designs, in: D.C. Montgomery (Ed.) Design and analysis of experiments, Wiley, 2012, pp. 478-553.

[74] B. Shahriari, K. Swersky, Z. Wang, R.P. Adams, N.d. Freitas, Taking the Human Out of the Loop: A Review of Bayesian Optimization, P IEEE 104 (2016) 148-175.

[75] J.-B.D. Green, T. Fulghum, M.A. Nordhaus, A review of immobilized antimicrobial agents and methods for testing, Biointerphases 6 (2011) MR13-MR28.

[76] J. Harmsen, Chapter Thirteen - Scale-Up in Reactor Design, in: A.K. Coker, C.A. Kayode (Eds.) Modeling of Chemical Kinetics and Reactor Design, Gulf Professional Publishing, Woburn, 2001, pp. 1034-1081.

[77] N. Kockmann, M. Gottsponer, D.M. Roberge, Scale-up concept of single-channel microreactors from process development to industrial production, Chem Eng J 167 (2011) 718-726.

[78] N. Kockmann, D.M. Roberge, Scale-up concept for modular microstructured reactors based on mixing, heat transfer, and reactor safety, Chem Eng Process 50 (2011) 1017-1026.

[79] D.S. Dickey, Tackling Difficult Mixing Problems, Chem Eng Prog 111 (2015) 35-42.

[80] E.V. Rebrov, J.C. Schouten, M.H.J.M. de Croon, Single-phase fluid flow distribution and heat transfer in microstructured reactors, Chem. Eng. Sci. 66 (2011) 1374-1393.

[81] G. Towler, R. Sinnott, Chapter 7 - Capital Cost Estimating, Chemical Engineering Design, Butterworth-Heinemann, Boston, 2013, pp. 307-354.

[82] R.S. Weber, L.J. Snowden-Swan, The economics of numbering up a chemical process enterprise, Int J Adv Manuf 1 (2019) e10011.

[83] A.M. Hiszpanski, B. Gallagher, K. Chellappan, P. Li, S. Liu, H. Kim, J. Han, B. Kailkhura, D.J. Buttler, T.Y.-J. Han, Nanomaterial Synthesis Insights from Machine Learning of Scientific Articles by Extracting, Structuring, and Visualizing Knowledge, J Chem Inf Mod 60 (2020) 2876-2887.